



Sproules, S. (2021) Oxo versus sulfido coordination at tungsten: a spectroscopic and correlated ab initio electronic structure study. *Inorganic Chemistry*, 60(12), pp. 9057-9063.

(doi: [10.1021/acs.inorgchem.1c01055](https://doi.org/10.1021/acs.inorgchem.1c01055))

There may be differences between this version and the published version. You are advised to consult the publisher's version if you wish to cite from it.

Copyright © 2021 Association for Computing Machinery. This is the author's version of the work. It is posted here for your personal use. Not for redistribution. The definitive Version of Record was published in *Inorganic Chemistry*, 60(12), pp. 9057-9063.

<https://eprints.gla.ac.uk/242758/>

Deposited on: 28 May 2021

Enlighten – Research publications by members of the University of
Glasgow
<http://eprints.gla.ac.uk>

Oxo versus Sulfido Coordination at Tungsten: A
Spectroscopic and Correlated Ab initio Electronic
Structure Study

*Stephen Sproules**

WestCHEM, School of Chemistry, University of Glasgow, Glasgow G12 8QQ, United Kingdom

Abstract. The tungsten ion that resides at the active site of a unique class of enzymes only found in esoteric hyperthermophilic archaea bacteria are known to possess at least one terminal chalcogenide ligand. The identity of this is either an oxo or sulfido (or both) is difficult to ascertain from structural studies, therefore small molecule analogues are developed to calibrate and substantiate spectroscopic signatures obtained from native proteins. The electronic structures of Tp^*WECl_2 ($\text{E} = \text{O}, \text{S}$; $\text{Tp}^* =$ hydrotris(3,5-dimethylpyrazol-1-yl)borate) have been scrutinized using electronic, EPR and X-ray absorption spectroscopy to assess the impact the terminal chalcogen on the *cis* chloride ligands. Examination at the Cl K-edge provides a direct probe of the bonding and therein lability of the chloride ligands, and in conjunction with density functional theoretical and multireference calculations, reveals greater bond covalency in Tp^*WOCl_2 compared to $\text{Tp}^*\text{WScCl}_2$. The computational model and electronic structure assignment is corroborated by reproduction of the spin-Hamiltonian parameters, whose magnitude is dominated by the sizeable spin-orbit coupling of tungsten.

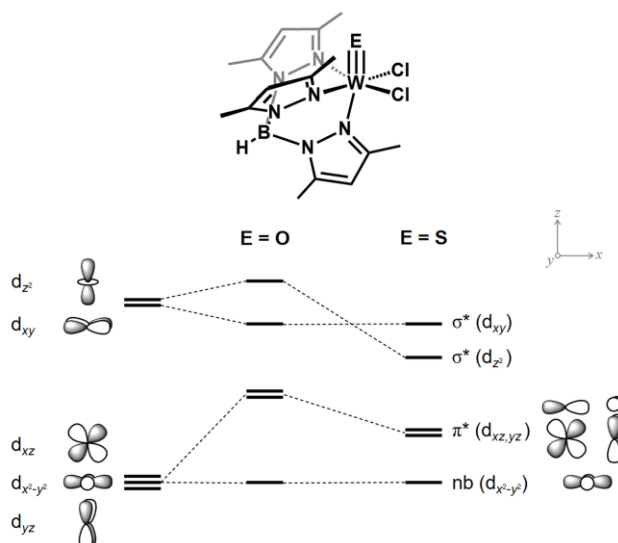
Introduction

True tungsten enzymes are defined as proteins that can only function with the third-row transition metal.^{1,2}

Nearly all of these enzymes have been found in prokaryotic hyperthermophilic archaea, which are some of the most ancient lifeforms on Earth.³ They are found in and around deep sea thermal vents in an euxinic environment that is sulfur-rich, devoid of oxygen, and representative of the climate several million years ago. The existence of tungstoenzymes in these archaea stands in contrast to the widespread use of its group 6 congener molybdenum that is found in all other life. Based on age, it is proposed that tungsten proteins came first, and the switch to molybdenum was made as the biosphere transitioned from a reducing environment to an oxidizing one. This postulation is underscored by the chemical similarity of tungsten and molybdenum, and both use the unique tricyclic pyranopterin cofactor which binds to the metal through a dithiolene chelate.^{4,5} As a result much of our knowledge of tungstoenzymes comes from examination of their more widespread molybdenum isoenzymes, which are less sensitive and more easily isolated and structurally characterized. Both catalyze two-electron transfer reactions that result in the net transfer of an oxygen atom, where the metal cycles through the +VI/V/IV oxidation states.⁶

Tungstoenzymes are categorized into two groups. The first are aldehyde oxidoreductases (AOR), which are the true enzymes harvested from the hyperthermophilic archaea.⁷ The second group are formate dehydrogenases (FDH) which are so profoundly similar to molybdenum enzymes, they are often considered part of the DMSO reductase group of enzymes.⁸ Such is the similarity of FDH and DMSO reductases that they continue to function regardless of the metal employed.⁹ In all tungstoenzymes the metal is coordinated by two pyranopterin dithiolenes with the remaining sites occupied by monodentate ligands ranging from oxide and sulfide to amino acid residues like cysteine and selenocysteine.^{4,10} While the cofactor is seen in the structural analysis, lighter atoms are not readily identified by X-ray diffraction

and absorption techniques, and there remains much speculation about the remaining ligands, which may be altered during purification and sampling.



Scheme 1. Structures of the Tp^*WECl_2 ($E = \text{O}, \text{S}$) compounds under study, and comparative ligand field splitting in oxo- and sulfido-tungsten moieties with C_{2v} symmetry labels.

The chemical similarity of molybdenum and tungsten diverges when considering their bonding to chalcogenides. Comparing just the tetrachalcogenide ions, ME_4^{2-} ($M = \text{Mo}, \text{W}; E = \text{O}, \text{S}$), molybdate is the most stable and soluble form of molybdenum in the sea, whereas it is tetrathiotungstate that has the higher solubility and availability in an euxinic environment. The tungsten-sulfido bond is more robust than for molybdenum, and it is highly likely that $\text{S}^{2-}/\text{SH}^-$ completes the coordination sphere in the AOR enzymes. It was recently shown that a terminal sulfido ligand is essential in the operation of molybdenum and tungsten FDHs.¹¹ Here the electronic effects of a terminal sulfido ligand is contrasted to an oxo in isostructural Tp^*WECl_2 complexes, where Tp^* is the hydrotris(3,5-dimethylpyrazol-1-yl)borate ligand,^{12,13} in a combined spectroscopic and computational study (Scheme 1). X-ray absorption spectroscopy (XAS) at the chlorine K-edge reveals the impact of the different terminal chalcogenide on

the two chloride ligands that are in an identical *cis* arrangement as the monodentate ligands that complete the coordination sphere in enzymes.¹⁴ The motivation for this study stems from the observation that these halides are more easily substituted for alkoxide/thiolate/selenolate ligands when adjacent a terminal sulfido.^{12,15-17} In contrast, ligand substitution at the equivalent oxotungsten center requires several days at refluxing temperature.^{13,18} The results show the more robust oxotungsten(V) center provides for a more covalent interaction with the two chloride ligands that is absent in the sulfidotungsten(V) analogue. Theoretical calculations are used to validate and quantify the subtle electronic structure factors that distinguish each terminal chalcogenide through accurate reproduction of the experimental observables in the EPR, electronic and X-ray absorption spectra.

Experimental Section

Synthesis of Complexes. The complexes Tp^*WOCl_2 and $\text{Tp}^*\text{WScCl}_2$ were synthesized according to literature procedures.^{12,13}

Chlorine K-edge X-ray Absorption Spectroscopy. All data were measured at the Stanford Synchrotron Radiation Lightsource (SSRL) under ring conditions of 3.0 GeV and 400 mA. Cl K-edge data were measured using the 54-pole wiggler beam line 4-3 in a high-magnetic field mode of 10 kG with a Ni-coated harmonic rejection mirror and a fully tuned Si(111) double-crystal monochromators. Details of the optimization of this setup for low-energy have been previously described.¹⁹ All samples were measured at room temperature as fluorescence spectra using a Lytle detector. Samples were ground finely and dispersed as thinly as possible on Mylar tape to minimize the possibility of fluorescence saturation effects. Data represent 3–4 scan averages measured for each sample over the 2740 – 2900 eV energy range. All

samples were monitored for photoreduction throughout the course of data collection. The incident X-ray energy was calibrated with reference to the spectrum of a solid anhydrous sodium thiosulfate ($\text{Na}_2\text{S}_2\text{O}_3$) standard using the literature value of 2469.2 eV as the energy of the lowest energy K-edge absorption peak.²⁰ A step size of 0.08 eV was used over the edge region. Data were averaged, and a smooth background was removed from all spectra by fitting a polynomial to the pre-edge region and subtracting this polynomial from the entire spectrum. Normalization of the data was accomplished by fitting a flattened polynomial or straight line to the post-edge region and normalizing the post-edge to 1.0. Fits to the pre-edges, modelled by pseudo-Voigt lines, were carried out using the program EDG_FIT with a fixed 1:1 ratio of Lorentzian to Gaussian contributions.²¹

Other Physical Methods. Electronic absorption spectra were obtained on a Perkin-Elmer Lambda 2 spectrophotometer (range 250 – 1100 nm). Continuous wave X-band EPR spectra was recorded on a Bruker ELEXSYS E500 spectrometer. The spectra were simulated with the Bruker XSOPHE suite.²² Frozen solution spectra were simulated following the spin Hamiltonian $\hat{H} = \mu_B \cdot \mathbf{g} \cdot \mathbf{B} \cdot \mathbf{S} + \Sigma \mathbf{S} \cdot \mathbf{A} \cdot \mathbf{I}$, where \mathbf{g} and \mathbf{A} are the 3×3 electron Zeeman and magnetic hyperfine interaction matrices, respectively. A Gaussian lineshape and distribution of g - and A -values (strain) were employed to account for the linewidth variation.

Calculations. The program package ORCA was used for density functional theory (DFT) calculations.²³ Geometry optimization employed the BP86 generalized gradient approximation functional,²⁴ single-point calculations on optimized and crystallographic coordinates used the one-parameter hybrid variant B3LYP.²⁵ The segmented all-electron relativistically contracted SARC-ZORA-def2-TZVPP basis set is used for tungsten, and ZORA-def2-TZVPP for all other atoms.²⁶ Auxiliary basis sets used to expand the

electron density in the calculations were chosen to match the orbital basis.²⁷ The RIJCOSX algorithm was used to speed the calculation of Hartree–Fock exchange.²⁸ Increased integration accuracy was applied to tungsten (grid = 10). Calculations included the zeroth-order regular approximation (ZORA) for relativistic effects²⁹ as implemented by van Wüllen.³⁰ The self-consistent field calculations were tightly converged ($1 \times 10^{-8} E_h$ in energy, $1 \times 10^{-7} E_h$ in the charge density, and 1×10^{-7} in the maximum element of the DIIS³¹ error vector). The geometry was converged with the following convergence criteria: change in energy $< 10^{-5} E_h$, average force $< 5 \times 10^{-4} E_h \text{ Bohr}^{-1}$, and the maximum force $10^{-4} E_h \text{ Bohr}^{-1}$. The geometry search for all complexes was carried out in redundant internal coordinates without imposing geometry constraints.

The property calculations at the optimized geometries with enhanced integration accuracy (SPECIALGRIDINTACC 16) for the tungsten atom. Calculation of the **g**-matrix included a larger the integration grid (Grid7), fully decontracted basis sets,³² and dichloromethane as solvent.³³ Time-dependent (TD-DFT) calculations of the chlorine K-pre-edges using the BP86 functional were performed as previously described.¹² Due to the limitations in the accurate treatment of excited states in DFT, absolute transition energies cannot be obtained by this method. Nevertheless, the relative transition energies and the relative intensities are, in general, reliably modelled. The chlorine 1s orbitals were localized using the Pipek–Mezey criteria,³⁴ and the TD-DFT equations³⁵ were solved individually for each chlorine atom, excluding all but excitations originating from the 1s orbital. It was established that a constant shift of +33.68 eV was required for this regime of basis sets and applied to the transition energies to align calculated and experimental data. Plots were obtained using a line broadening of 1.0 eV.

Correlated post-Hartree-Fock ab initio calculations were performed on TpWOCl_2 and TpWScI_2 where Tp is hydrotris(pyrazol-1-yl)borato ligand sans methyl substituents. The methyl groups were truncated, and the hydrogen atoms optimized using the BP86 functional. The state-averaged complete active space

self-consistent field (SA-CASSCF) method³⁶ with a SARC-ZORA-TZVPP basis set for tungsten and ZORA-def2-TZVPP basis set for all other atoms. A CASSCF(9,9) – nine electrons in nine active orbitals – calculation was performed, and averaged over 20 doublet states. The NEVPT2 calculations were performed on each reference space.³⁷ In the case of the CASSCF/NEVPT2 method, the matrix elements are obtained with the CASSCF wavefunctions and only the diagonal energies contain the dynamic correlation brought in by the NEVPT2 procedure. Molecular orbitals and spin density maps were visualized via the program Molekel.³⁸

Results and Discussion

The reaction of colorless $\text{Tp}^*\text{WO}_2\text{Cl}$ with BCl_3 in refluxing toluene produces sky blue Tp^*WOCl_2 .¹³ Direct conversion to $\text{Tp}^*\text{WScCl}_2$ can be achieved with boron sulfide, though treating a dichloromethane solution of $\text{Tp}^*\text{WS}_2\text{Cl}$ with triphenylphosphine generates the sulfido analogue in higher yield.¹² For Tp^*WOCl_2 there is a crystal structure, though the metrics are of limited value on account of the crystallographic mirror plane that disorders the position of the oxo ligand with one of the chlorides.³⁹ The same disorder befell $\text{Tp}^*\text{WScCl}_2$ and related dichalcogenides $\text{Tp}^*\text{WE}_2\text{Cl}$ (E = O, S), and only extended X-ray absorption fine structure (EXAFS) analysis at the W L_3 -edge could distinguish the facial arrangement of these similarly sized ligands.¹⁶

The electronic spectra of Tp^*WOCl_2 and $\text{Tp}^*\text{WScCl}_2$ overlaid in Figure 1 are characterized by a weakly intense ligand field (LF) band. For the sky blue complex, the peak at $15\,650\text{ cm}^{-1}$ ($\epsilon = 66\text{ M}^{-1}\text{ cm}^{-1}$) bears a shoulder on the low energy side at $14\,200\text{ cm}^{-1}$ (Table 1). This is assigned as the $d_{x^2-y^2} \rightarrow d_{xz,yz}$ excitation, where the 1450 cm^{-1} separation is a measure of the inequivalence of the $\text{W}=\text{O}$ π^* orbitals brought about by relatively strong *N*-donor atoms on one side and weak field chlorides on the other.¹³ The corresponding transition in $\text{Tp}^*\text{WScCl}_2$ is shifted into the near-infrared region at $10\,250\text{ cm}^{-1}$, which is consistent with

the weaker field of the sulfido ligand compared to its oxo counterpart (Scheme 1).¹² The exact same difference is seen for the molybdenum analogues, though both are red-shifted by $\sim 1300\text{ cm}^{-1}$ for the second-row metal.⁴⁰

The dark yellow color of Tp^*WCl_2 stems from the absorption at $24\,150\text{ cm}^{-1}$, and based on computational reproduction of the spectrum, this feature is ascribed as a ligand-to-metal charge transfer (LMCT) transition from the $\text{W}=\text{S}\ \pi$ orbitals to the $\text{W}=\text{S}\ \pi^*$ acceptor orbitals.

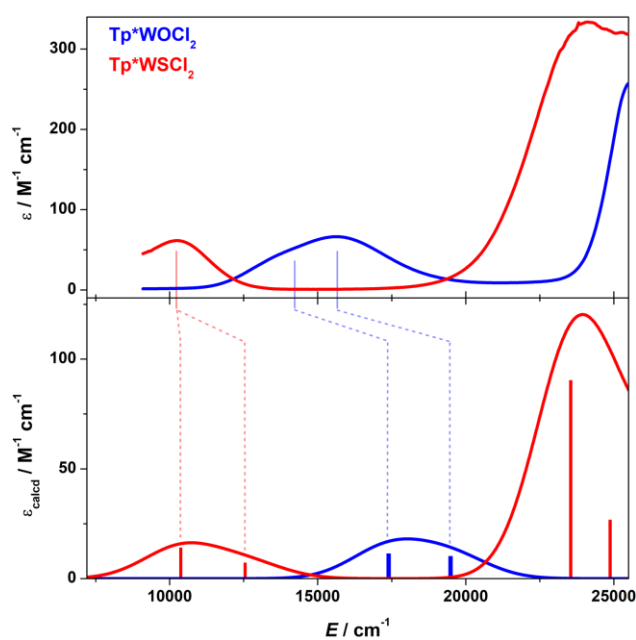


Figure 1. Overlay of the experimental electronic spectra of Tp^*WOCl_2 and Tp^*WCl_2 recorded in dichloromethane solution (top) and the SA-CASSCF/NEVPT2 calculated spectra (bottom). Vertical lines represent experimental and calculated transitions.

Table 1. Experimental and Calculated Electronic and X-ray Absorption Spectroscopic Data

	Electronic ^a			Cl K-edge ^b		
	exptl	calcd ^c	assignment	exptl	calcd ^d	assignment
Tp*WOCl ₂	14 225	17395	d _{x²-y²} → d _{yz} (π*)	2817.1	2817.0	1s → d _{x²-y²}
	15 650	19488	d _{x²-y²} → d _{xz} (π*)	2818.2	2817.8	1s → d _{xz,yz} (π*)
				2819.8	2819.8	1s → d _{xy}
Tp*WScI ₂	10 235	10376	d _{x²-y²} → d _{xz} (π*)	2817.1	2817.1	1s → d _{x²-y²}
		12549	d _{x²-y²} → d _{yz} (π*)			1s → d _{xz,yz} (π*)
	24155	23545	W=S π → d _{xz,yz} (π*)	2819.6	2819.7	1s → d _{z²} (σ*)
		24875	W=S π → d _{z²} (σ*)			1s → d _{xy}

^a Transition energies in cm⁻¹. ^b Transition energies in eV. ^c From SA-CASSCF/NEVPT2 calculations. ^d From B3LYP/SARC-ZORA-TZVPP TD-DFT calculations.

EPR spectroscopy. The presence of paramagnetic W(V) d¹ ions in Tp*WOCl₂ and Tp*WScI₂ has been confirmed by EPR (Figure 2). The isotopic *g*-values of 1.802 and 1.731, respectively, are consistent with change in ligand field strengths of the terminal chalcogenide.^{12,13} Unlike the room temperature measurement, the frozen solution spectrum recorded at 130 K in a CH₂Cl₂/DMF glass resolved hyperfine splitting from coupling to the ¹⁸³W nucleus (*I* = 1/2, 14.3% abundant) with observable features at the perimeter of the spectrum. Both spectra are rhombic, with the principal *g*-values far removed from that of the free electron (*g*_e = 2.0023) commensurate with a W(V) ion with weak equatorial ligands (Table 2).⁴¹

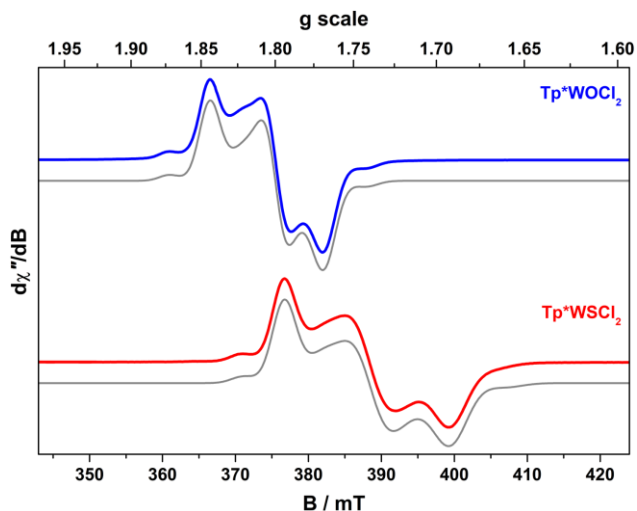


Figure 2. Comparison of the X-band EPR spectra of Tp^*WOCl_2 and Tp^*WSCl_2 in $\text{CH}_2\text{Cl}_2/\text{DMF}$ solution at 130 K (experimental conditions: frequency, 9.459 GHz; power, 0.63 mW; modulation, 0.5 mT). Simulations are represented by the gray trace.

Simulation revealed an axial hyperfine interaction where the largest A -value is aligned with the smallest g -value. As these complexes are orthorhombic with pseudo- C_{2v} symmetry, it requires that only g_y and A_y be coincident and perpendicular to the mirror plane that bisects the chloro ligands. Hence Euler angles of 44° for Tp^*WOCl_2 and 27° for Tp^*WSCl_2 were introduced to achieve an accurate simulation. These are similar in magnitude to the molybdenum analogues, where the larger value is applied to the oxo complex.⁴⁰ The angle defines the rotation of g_x and g_z away from A_x and A_z brought about by the admixture of d_{xz} orbital into the ground state $d_{x^2-y^2}$ orbital. This leads to titling of the $d_{x^2-y^2}$ orbital away from the chloro ligands such that it is no longer perfectly orthogonal to the $\text{W}=\text{E}$ bond, though both g_z and A_z are still mostly aligned with this bond. The magnitude of the rotation angle dictates the d_{xz} content in the ground state, and as this orbital is projected towards the chlorides, induces a π interaction that stabilises these equatorial ligand bonds.⁴²

Table 2. Experimental and Calculated Spin-Hamiltonian Parameters^a

	g_x	g_y	g_z	$\langle g \rangle^b$	Rhombicity ^c	A_x	A_y	A_z	$\langle A \rangle^d$	β^e
Tp*WOCl ₂										
experiment	1.8441	1.7994	1.7679	1.8038	0.59	-61	-64	-116	-80	44°
DFT ^f	1.9173	1.8220	1.7779	1.8391	0.68	-79	-81	-113	-91	37°
NEVPT2 ^g	1.8217	1.8191	1.5123	1.7177	0.01					
Tp*WScCl ₂										
experiment	1.7874	1.7353	1.6862	1.7363	0.51	-78	-73	-128	-93	27°
DFT ^f	1.9195	1.7425	1.7051	1.7890	0.83	-81	-82	-113	-92	34°
NEVPT2 ^g	1.7156	1.7032	1.4825	1.6338	0.05					
Tp*MoOCl ₂ ^h	1.971	1.941	1.934	1.949	0.81	71.4	18.1	38.1	42.5	33°
Tp*MoScCl ₂ ^h	1.941	1.921	1.919	1.927	0.91	70.7	18.0	41.2	43.3	31°

^a A-values in $\times 10^{-4} \text{ cm}^{-1}$; the sign is negative owing to the dominant Fermi-contact contribution. ^b $\langle g \rangle = (g_x + g_y + g_z)/3$. ^c Rhombicity = $(g_x - g_y)/(g_x - g_z)$. ^d $\langle A \rangle = (A_x + A_y + A_z)/3$. ^e Euler angle defined as rotation of A-matrix about g_y . ^f From B3LYP/SARC-ZORA-TZVPP DFT calculations. ^g From SA-CASSCF/NEVPT2 calculations. ^h Data taken from ref. 40.

The spectral profile of Tp*WEC₂ follow the ligand field prediction of a near-axial d¹ system where $g_e > g_\perp (= g_{x,y}) > g_\parallel (= g_z)$.⁴³ The same pattern was observed for Tp*MoOF₂ but crucially not for Tp*MoOCl₂ and Tp*MoOBr₂, where the trend is inverted as $g_\parallel > g_\perp$.^{42,44} Overall the Tp*MoECl₂ analogues are more axial than the tungsten counterparts, where the largest hyperfine component corresponds to the largest g -value (Table 2). This pattern is independent of the terminal chalcogenide ligand. The shift in g_\parallel is governed by in-plane covalency and spin-orbit coupling contributions from the halide ligands, and suggests a less covalent chloride bond exists for tungsten, where g -anisotropy is dominated by spin-orbit coupling from tungsten. Assessing the input for the terminal chalcogenide, in-plane covalency is lower for Tp*WScCl₂ than Tp*WOCl₂ as it has the smaller Euler angle and more rhombic g -values.

X-ray absorption spectroscopy. The chlorine K-edge spectra presented in Figure 3 allow for a direct comparison of the orbital manifolds of the $\{\text{WO}\}^{3+}$ and $\{\text{WS}\}^{3+}$ centers. For Tp^*WOCl_2 , three pre-edge peaks at 2817.1, 2818.2 and 2819.8 eV are assigned as dipole-allowed transitions from the Cl 1s orbital to vacancies in the $d_{x^2-y^2}$, $d_{xz,yz}$ and d_{xy} orbitals as they each possess some Cl 3p character (Table 1). The peak for an excitation to the $\text{W}=\text{O}$ σ^* (d_z^2) orbital resides at an energy beyond the $1s \rightarrow 4p$ rising edge (>2820.5 eV). By contrast, the spectrum of Tp^*WCl_2 has two pre-edge peaks, resulting from overlapping excitations to the $d_{x^2-y^2}$ and $d_{xz,yz}$ orbitals at 2817.1 eV, and the d_z^2 and d_{xy} orbitals at 2819.6 eV, highlighting the weaker π -donation of the sulfido ligand that stabilizes the π^* and σ^* orbitals compared to the oxo species (Scheme 1).

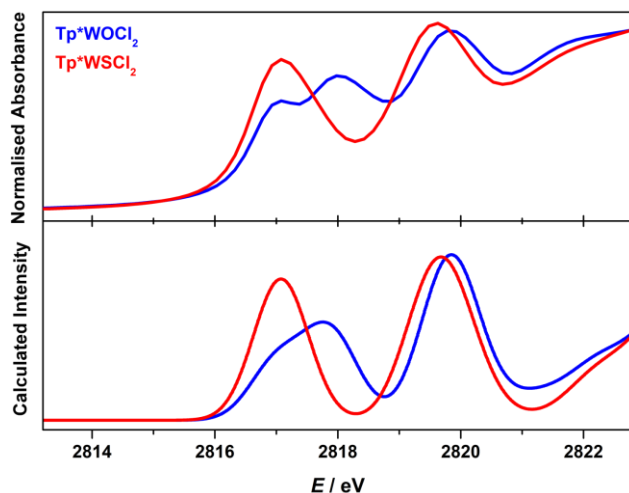


Figure 3. Overlay of the experimental (top) and calculated (bottom) Cl K-edge spectra for Tp^*WOCl_2 and Tp^*WCl_2 obtained from ZORA-B3LYP TD-DFT calculations. Calculated intensity in arbitrary units.

Pseudo-Voigt deconvolution confirms the $1s \rightarrow d_{x^2-y^2}$ transition is at 2817.1 eV for both complexes, consistent with their similar reduction potentials (Tp^*WOCl_2 : -1.30 V; Tp^*WCl_2 : -1.24 V vs $\text{Fc}^{+/0}$).^{12,13}

The difference in energy between the first and second peaks is 1.1 eV for the oxo complex and estimated at 0.7 eV for the sulfido species. Thus the W=S π^* orbitals are stabilized by $\sim 3,000\text{ cm}^{-1}$, compared to $5,450\text{ cm}^{-1}$ from electronic absorption spectroscopy (Figure 1). The next peak in Tp*WOCl₂ (2819.8 eV) and the second band in Tp*WScCl₂ (2819.6 eV) are dominated by the excitation to the W–Cl σ^* orbital, whose energy is independent of the terminal chalcogenide ligand. The d_{xy} orbital is $>20\,000\text{ cm}^{-1}$ above the ground state as measured by Cl K-edge, and consistent with the $\sim 25\,000\text{ cm}^{-1}$ lower limit ascertained from electronic and sulfur K-edge XAS (Figure S10).¹²

Theoretical Calculations. Charge-neutral Tp*WOCl₂ and Tp*WScCl₂ were optimized in the gas phase using the BP86 functional. In both structures the W–Cl distances are identical at 2.356 Å, with a short W–S distance of 2.144 Å and shorter W–O bond at 1.711 Å (Table S3). These distances are an excellent match to structurally characterized sulfido- and oxo-tungsten(V) complexes with the Tp* ligand.^{12,13} One W–N distance is ca. 0.2 Å longer than the other two, and is a consequence of the trans influence well documented in terminal chalcogenide complexes. This is larger for Tp*WOCl₂ where the W ion resides 0.26 Å out of the N₂Cl₂ equatorial plane, which increases to 0.31 Å in Tp*WScCl₂.

The ground state electronic structures, computed at the B3LYP level of theory, produced the ligand field splitting as shown in Scheme 1. This model is validated by the very accurate reproduction of the Cl K-pre-edge using time-dependent (TD)-DFT calculations (Figure 3). Applying the constant shift of +33.68 eV, the first and last pre-edge peaks are calculated to be within 0.1 eV of the experimental values (Table 1). The largest deviation is for the transition to the $d_{xz,yz}$ (W=E π^*) which are underestimated by 0.4 eV for Tp*WOCl₂ and ~ 0.5 eV for Tp*WScCl₂ where the calculated peak is narrower than the experimental one (Figures S8 and S9). The excellent match of relative intensities of the peaks reflects the Cl 3p content to the predominantly W 5d acceptor orbitals (Table S4), with the salient observation being the 11.9%

contribution to the ground state orbital of Tp^*WOCl_2 compared to 10.4% in TpWScCl_2 . The Cl contribution arises from an in-plane π interaction with the $d_{x^2-y^2}$ orbital, and dictated by the E–W–Cl bond angles which modulate the alignment of the in-plane Cl p orbitals.

A more rigorous correlated post-Hartree-Fock ab initio calculation was performed using a CAS(9,9) reference with nine electrons in the nine orbitals as the largest manageable active space. This encompasses the five d orbitals and the W=E σ and π , and W–Cl σ bonding counterparts (Figures S4 and S5). Electronic properties for both complexes were computed for 20 doublet states. The lowest energy LF band for Tp^*WOCl_2 was estimated 3000–4000 cm^{-1} above the experimental peak though the calculation produced the correct energetic splitting of the d_{xz} and d_{yz} orbitals at 2100 cm^{-1} compared with 1300 cm^{-1} experimentally (Figure 1). The accuracy of this estimate is likely due to the differences in the structure of the molecule in solution and the influence of solvation on the first coordination sphere, which is not included in the geometry optimization. No other transition was calculated in the visible region. The analogous transitions for $\text{Tp}^*\text{WScCl}_2$ were calculated at 10 400 and 12 550 cm^{-1} , a closer match with the experimental data (Table 1). The energetic splitting of the d_{xz} and d_{yz} orbitals is estimated at 2175 cm^{-1} , essentially identical to Tp^*WOCl_2 . The band at 24 150 cm^{-1} that gives $\text{Tp}^*\text{WScCl}_2$ its color is assigned as a $\pi \rightarrow \pi^*$ LMCT transition within the W=S unit. The shift to lower energy is due to the poorer π -donor ability of the sulfido ligand.

EPR spin-Hamiltonian parameters were calculated using both DFT and ab initio methods (Table 2). The latter provides a more accurate treatment of relativistic effects and spin-orbit coupling which is the dominant contribution to the g -values. The SA-CASSCF/NEVPT2 calculated g -values reproduce the experimental $g_{\perp} > g_{\parallel}$ pattern, with a very good match for g_x and g_y as these shift based on mixing of the $d_{xz,yz}$ orbitals into the ground state via spin-orbit coupling. The limited size of the active space is evident in the rhombicity of the calculated spectrum. Firstly, the calculated g -values for Tp^*WOCl_2 and

Tp*WScCl₂ are highly axial with $g_x \approx g_y$, and g_z considerably lower than seen in the experiment. Westmoreland and co-workers have meticulously examined the contributions to the g -shifts in analogous oxomolybdenum(V) complexes, and revealed the magnitude of g_z is governed by equatorial metal-ligand covalency, the size of these ligands, and low-energy charge transfer states.^{42,44} The analysis successfully accounted for the observed shift of g_z above g_{\perp} and g_e in molybdoenzymes and model complexes.¹⁴ The low g_z value computed here is a result of an absence of several predominantly chlorine-based orbitals whose CT contributions would increase g_z . That aside, it does show the lack of covalency in the W–Cl bonds compared with alkoxide, thiolate, selenolate ligands. Thus halides are a poor representation of the pyranopterindithiolene cofactor that remains coordinated and more like the amino acid residues, substrates or solvent molecules that can detach from the metal ion during enzymatic operation.^{2,9} As DFT provides a less rigorous treatment of relativistic effects, it underestimates the g -shifts, most notably for g_x (Table 2). This is an inherent drawback of DFT, though Kaupp and co-workers have recently presented improved methodology to handling spin-orbit effects in heavy elements.⁴⁵ On the other hand, DFT gives excellent match to the hyperfine coupling constants in terms of the magnitude of the A -values and their axial splitting, as well as the Euler angles of 37° and 34° for Tp*WOCl₂ and Tp*WScCl₂, respectively. The larger hyperfine interaction in the latter reflects a greater localization of the unpaired spin on the tungsten ion and a less covalent $d_{x^2-y^2}$ ground state.

Conclusions

The combined spectroscopic and computational analysis of a pair of isoelectronic and isostructural complexes reveal the subtle electronic impact of the terminal chalcogenide – oxo vs. sulfido – on the bonding of two *cis* chloride ligands. The chlorides are representative of labile ligands such as the substrate or solvent that are displaced in the course of catalytic turnover at the metalloenzyme center. Their

interaction with the oxo- and sulfido-tungsten(V) is directly probed using Cl K-edge XAS, which in combination with a TD-DFT reproduction of the pre-edge spectrum, revealed a more covalent W–Cl interaction in Tp*WOCl₂ than Tp*WScCl₂, as quantified by the Cl 3p contribution to the d_{x²-y²} ground state orbital. The effect is subtle, with ~10% more covalency in the oxotungsten(V) complex that contribute to the observed inertness of Tp*WOCl₂ toward ligand exchange. In contrast, the chloride ligands in Tp*WScCl₂ are more labile and suggests that for enzymes where substrates are bound to the tungsten center, a terminal sulfido provides a more favorable pathway. This lends credence to the likelihood that sulfur atom transfer processes are operative in tungstoenzymes in contrast to the oxygen atom transfer in molybdoenzymes.¹⁵ The two-step process would see oxidation of the substrate by sulfide followed by hydrolysis outside the protein, which might be the thermodynamically preferred route given the unique climate in which these enzymes reside.

ASSOCIATED CONTENT

Supporting Information

The Supporting Information is available free of charge at <https://pubs.acs.org/doi/10.1021/acs.inorgchem.xxxxxxx>.

Additional spectra, and computational data including optimized coordinates, charge and spin density populations and reduced orbital analyses (PDF).

AUTHOR INFORMATION

Corresponding Author

Stephen Sproules – *WestCHEM, School of Chemistry, University of Glasgow, Glasgow G12 8QQ, United Kingdom*; orcid.org/0000-0003-3587-0375; E-mail: stephen.sproules@glasgow.ac.uk

Notes

The author declares no competing financial interest.

ACKNOWLEDGMENT

This work is dedicated to the memory of Professor Richard H. Holm for his seminal contribution to molybdenum and tungsten bioinorganic chemistry. The work is supported by the University of Glasgow, and the Scottish Funding Council for a Postgraduate and Early Career Researcher Exchange (PECRE) grant.

REFERENCES

1. Maia, L. B.; Moura, I.; Moura, J. J. G. In *Molybdenum and Tungsten Enzymes: Biochemistry*; Hille, R., Schulzke, C., Kirk, M. L., Eds.; The Royal Society of Chemistry: UK, 2017, p 1.
2. Hagen, W. R. In *Molybdenum and Tungsten Enzymes: Biochemistry*; Hille, R., Schulzke, C., Kirk, M. L., Eds.; The Royal Society of Chemistry: UK, 2017, p 313.
3. (a) Johnson, M. K.; Rees, D. C.; Adams, M. W. W. Tungstoenzymes. *Chem. Rev.* **1996**, *96*, 2817. (b) Andreesen, J. R.; Makedessi, K. Tungsten, the Surprisingly Positively Acting Heavy Metal Element for Prokaryotes. *Ann. N.Y. Acad. Sci.* **2008**, *1125*, 215.
4. Hille, R. The Molybdenum Oxotransferases and Related Enzymes. *Dalton Trans.* **2013**, *42*, 3029.
5. Pushie, M. J.; Cotelesage, J. J.; George, G. N. Molybdenum and Tungsten Oxygen Transferases - Structural and Functional Diversity within a Common Active Site Motif. *Metallomics* **2014**, *6*, 15.

6. Sugimoto, H.; Tsukube, H. Chemical Analogues Relevant to Molybdenum and Tungsten Enzyme Reaction Centres Toward Structural Dynamics and Reaction Diversity. *Chem. Soc. Rev.* **2008**, *37*, 2609.
7. Arndt, F.; Schmitt, G.; Winiarska, A.; Saft, M.; Seubert, A.; Kahnt, J.; Heider, J. Characterization of an Aldehyde Oxidoreductase From the Mesophilic Bacterium *Aromatoleum aromaticum* EbN1, a Member of a New Subfamily of Tungsten-Containing Enzymes. *Front. Microbiol.* **2019**, *10*, 71.
8. (a) Wagner, T.; Ermler, W.; Shima, S. The Methanogenic CO₂ Reducting-and-Fixing Enzyme is Bifunctional and Contains 46 [4Fe-4S] Clusters. *Science* **2016**, *354*, 114. (b) Hille, R. Molybdenum and Tungsten in Biology. *Trends Biochem. Sci.* **2002**, *27*, 360.
9. Nicks, D.; Hille, R. Molybdenum- and Tungsten-containing Formate Dehydrogenases and Formylmethanofuran Dehydrogenases: Structure, Mechanism, and Cofactor Insertion. *Protein Sci.* **2018**, *28*, 111.
10. (a) Pushie, M. J.; Cotelesage, J. J.; George, G. N. Molybdenum and tungsten oxygen transferases – structural and functional diversity within a common active site motif. *Metallomics* **2014**, *6*, 15. (b) Holm, R. H.; Solomon, E. I.; Majumdar, A.; Tenderholt, A. L. Comparative molecular chemistry of molybdenum and tungsten and its relation to hydroxylase and oxotransferase enzymes. *Coord. Chem. Rev.* **2011**, *255*, 993. (c) Jiang, J.; Holm, R. H. An Expanded Set of Functional Groups in Bis(dithiolene)tungsten(IV,VI) Complexes Related to the Active Sites of Tungstoenzymes, Including W^{IV}–SR and W^{VI}–O(SR). *Inorg. Chem.* **2004**, *43*, 1302. (d) Sung, K.-M.; Holm, R. H. Synthesis and Structures of Bis(dithiolene)–Tungsten(IV) Complexes Related to the Active Sites of Tungstoenzymes. *Inorg. Chem.* **2000**, *39*, 1275. (e) Sung, K.-M.; Holm, R. H. Substitution and Oxidation Reactions of Bis(dithiolene)tungsten Complexes of Potential Relevance to Enzyme Sites. *Inorg. Chem.* **2001**, *40*, 4518.

11. (a) Schrapers, P.; Hartmann, T.; Kositzki, R.; Dau, H.; Reschke, S.; Schulzke, C.; Leimkühler, S.; Haumann, M. Sulfido and Cysteine Ligation Changes at the Molybdenum COfactor during Substrate Conversion by Formate Dehydrogenase (FDH) from *Rhodobacter capsulatus*. *Inorg. Chem.* **2015**, *54*, 3260. (b) Robinson, W. E.; Bassegoda, A.; Blaza, J. N.; Reisner, E.; Hirst, J. Understanding How the Rate of C–H Bond Cleavage Affects Formate Oxidation Catalysis by a Mo-Dependent Formate Dehydrogenase. *J. Am. Chem. Soc.* **2020**, *142*, 12226.
12. Sproules, S.; Eagle, A. A.; George, G. N.; White, J. M.; Young, C. G. Mononuclear Sulfido-Tungsten(V) Complexes: Completing the Tp*MEXY (M = Mo, W; E = O, S) Series. *Inorg. Chem.* **2017**, *56*, 5189.
13. Sproules, S.; Eagle, A. A.; Taylor, M. K.; Gable, R. W.; White, J. M.; Young, C. G. Paramagnetic Oxotungsten(V) Complexes Containing the Hydrotris(3,5-dimethylpyrazol-1-yl)borate Ligand. *Inorg. Chem.* **2011**, *50*, 4503.
14. Enemark, J. H.; Cooney, J. J. A.; Wang, J.-J.; Holm, R. H. Synthetic Analogues and Reaction Systems Relevant to the Molybdenum and Tungsten Oxotransferases. *Chem. Rev.* **2004**, *104*, 1175.
15. Eagle, A. A.; Gable, R. W.; Thomas, S.; Sproules, S. A.; Young, C. G. Sulfur Atom Transfer Reactions of Tungsten(VI) and Tungsten(IV) Chalcogenide Complexes. *Polyhedron* **2004**, *23*, 385.
16. (a) Eagle, A. A.; Harben, S. M.; Tiekink, E. R. T.; Young, C. G. Tungsten Bioinorganic Chemistry: Synthesis, Structure, and Reactivity of *cis*-Oxothio-tungsten(VI), *cis*-Bis(thio)tungsten(VI), and (Ene-1,2-dithiolato)tungsten(IV) Complexes. *J. Am. Chem. Soc.* **1994**, *116*, 9749. (b) Eagle, A. A.; Tiekink, E. R. T.; George, G. N.; Young, C. G. Synthesis, Characterization, and Electrochemistry of *cis*-Oxothio- and *cis*-Bis(thio)tungsten(VI) Complexes of Hydrotris(3,5-dimethylpyrazol-1-yl)borate. *Inorg. Chem.* **2001**, *40*, 4563.

17. Thomas, S.; Eagle, A. A.; Sproules, S. A.; Hill, J. P.; White, P. S.; Tiekink, E. R. T.; George, G. N.; Young, C. G. Redox Interplay of Oxo-Thio-Tungsten Centers with Sulfur-Donor Co-Ligands. *Inorg. Chem.* **2003**, *42*, 5909.
18. Eagle, A. A.; Tiekink, E. R. T.; Young, C. G. Dioxotungsten(VI) Complexes of Hydrotris(3,5-dimethylpyrazol-1-yl)borate Including the X-ray Crystal Structure of the Tungsten Selenophenolate Complex *cis*-{HB(Me₂C₃N₂H)₃}WO₂(SePh). *Inorg. Chem.* **1997**, *36*, 6315.
19. Hedman, B.; Frank, P.; Gheller, S. F.; Roe, A. L.; Newton, W. E.; Hodgson, K. O. *J. Am. Chem. Soc.* **1988**, *110*, 3798.
20. Sekiyama, H.; Kosugi, N.; Kuroda, H.; Ohta, T. Sulfur K-Edge Absorption Spectra of Na₂SO₄, Na₂SO₃, Na₂S₂O₃, and Na₂S₂O_x (*x* = 5 – 8). *Bull. Chem. Soc. Jpn.* **1986**, *59*, 575.
21. EXAFSPAK & EDG_FIT, Stanford Synchrotron Radiation Laboratory, Stanford Linear Accelerator Center, Stanford University, CA, 2000.
22. Hanson, G. R.; Gates, K. E.; Noble, C. J.; Griffin, M.; Mitchell, A.; Benson, S. XSophe-Sophen-XeprView[®]. A Computer Simulation Software Suite (v. 1.1.3) for the Analysis of Continuous Wave EPR Spectra. *J. Inorg. Biochem.* **2004**, *98*, 903.
23. Neese, F. The ORCA Program System. *WIREs Comput. Molec. Sci.* **2012**, *2*, 73.
24. (a) Tao, J. M.; Perdew, J. P.; Staroverov, V. N.; Scuseria, G. E. Climbing the Density Functional Ladder: Nonempirical Meta-Generalized Gradient Approximation Designed for Molecules and Solids. *Phys. Rev. Lett.* **2003**, *91*, 146401. (b) Becke, A. D. Density Functional Calculations of Molecular Bond Energies. *J. Chem. Phys.* **1988**, *84*, 4524. (c) Perdew, J. P. Density-Functional Approximation for the Correlation Energy of the Inhomogeneous Electron Gas. *Phys. Rev. B* **1986**, *33*, 8822.

25. (a) Becke, A. D. Density-Functional Thermochemistry. III. The Role of Exact Exchange. *J. Chem. Phys.* **1993**, *98*, 5648. (b) Lee, C. T.; Yang, W. T.; Parr, R. G. Development of the Colle-Salvetti Correlation-Energy Formula into a Functional of the Electron Density. *Phys. Rev. B* **1988**, *37*, 785.
26. (a) Pantazis, D. A.; Neese, F. All-Electron Scalar Relativistic Basis Sets for the Lanthanides. *J. Chem. Theory Comput.* **2009**, *5*, 2229. (b) Weigend, F.; Ahlrichs, R. Balanced Basis Sets of Split Valence, Triple Zeta Valence and Quadrupole Zeta Valence Quality for H to Rn: Design and Assessment of Accuracy. *Phys. Chem. Chem. Phys.* **2005**, *7*, 3297.
27. Weigend, F. Accurate Coulomb-Fitting Basis Sets for H to Rn. *Phys. Chem. Chem. Phys.* **2006**, *8*, 1057.
28. (a) Izsák, R.; Neese, F. An Overlap Fitted Chain of Spheres Exchange Method. *J. Chem. Phys.* **2011**, *135*, 144105. (b) Neese, F.; Wennmohs, F.; Hansen, A.; Becker, U. Efficient, Approximate and Parallel Hartree–Fock and hybrid DFT calculations. A ‘Chain-of-Spheres’ Algorithm for the Hartree–Fock Exchange. *Chem. Phys.* **2009**, *356*, 98.
29. (a) van Lenthe, E.; Snijders, J. G.; Baerends, E. J. The Zero–Order Regular Approximation for Relativistic Effects: The Effect of Spin–Orbit Coupling in Closed Shell Molecules. *J. Chem. Phys.* **1996**, *105*, 6505. (b) van Lenthe, E.; van der Avoird, A.; Wormer, P. E. S. Density Functional Calculations of Molecular Hyperfine Interactions in the Zero Order Regular Approximation for Relativistic Effects. *J. Chem. Phys.* **1998**, *108*, 4783. (c) van Lenthe, J. H.; Faas, S.; Snijders, J. G. Gradients in the ab initio Scalar Zeroth-Order Regular Approximation (ZORA) Approach. *Chem. Phys. Lett.* **2000**, *328*, 107.
30. van Wüllen, C. J. Molecular Density Functional Calculations in the Regular Relativistic Approximation: Method, Application to Coinage Metal Diatomics, Hydrides, Fluorides and Chlorides, and Comparison with First-Order Relativistic Calculations. *J. Chem. Phys.* **1998**, *109*, 392.

31. (a) Pulay, P. Convergence Acceleration of Iterative Sequences. The Case of SCF Iteration. *Chem. Phys. Lett.* **1980**, *73*, 393. (b) Pulay, P. Improved SCF Convergence Acceleration. *J. Comput. Chem.* **1982**, *3*, 556.
32. (a) Neese, F. Prediction of Electron Paramagnetic Resonance g Values using Coupled Perturbed Hartree–Fock and Kohn–Sham Theory. *J. Chem. Phys.* **2001**, *115*, 11080. (b) Neese, F. Metal and Ligand Hyperfine Couplings in Transition Metal Complexes: The Effect of Spin–Orbit Coupling as Studied by Coupled Perturbed Kohn–Sham Theory. *J. Chem. Phys.* **2003**, *118*, 3939.
33. Barone, V.; Cossi, M. Quantum Calculation of Molecular Energies and Energy Gradients in Solution by a Conductor Solvent Model. *J. Phys. Chem. A* **1998**, *102*, 1995.
34. Pipek, J.; Mezey, P. G. A Fast Intrinsic Localization Procedure Applicable for *ab initio* and Semiempirical Linear Combination of Atomic Orbital Wave Functions. *J. Chem. Phys.* **1989**, *90*, 4916.
35. Neese, F.; Olbrich, G. Efficient use of the Resolution of the Identity Approximation in Time-Dependent Density Functional Calculations with Hybrid Density Functionals. *Chem. Phys. Lett.* **2002**, *362*, 170.
36. (a) Roos, B. O.; Taylor, P. R.; Siegbahn, P. E. M. A Complete Active Space SCF Method (CASSCF) using a Density Matrix Formulated Super-CI Approach. *Chem. Phys.* **1980**, *48*, 157. (b) Siegbahn, P. E. M.; Heiberg, A.; Roos, B.; Levy, B. A Comparison of the Super-CI and the Newton-Raphson Scheme in the Complete Active Space SCF Method. *Phys. Scr.* **1980**, *21*, 323. (c) Siegbahn, P. E. M.; Almlöf, J.; Heiberg, A.; Roos, B. O. The Complete Active Space SCF (CASSCF) Method in a Newton–Raphson Formulation with Application to the HNO Molecule. *J. Chem. Phys.* **1981**, *74*, 2384.

37. (a) Angeli, C.; Cimiraglia, R. Introduction of n -Electron Valence States for Multireference Perturbation Theory. *J. Chem. Phys.* **2001**, *114*, 10252. (b) Angeli, C.; Cimiraglia, R.; Malrieu, J.-P. N -Electron Valence State Perturbation Theory: A Fast Implementation of the Strongly Contracted Variant. *Chem. Phys. Lett.* **2001**, *350*, 297. (c) Angeli, C.; Cimiraglia, R. Multireference perturbation Configuration Interaction V. Third-Order Energy Contributions in the Møller–Plesset and Epstein–Nesbet Partitions. *Theor. Chem. Acc.* **2002**, *107*, 313. (d) Angeli, C.; Cimiraglia, R.; Malrieu, J.-P. N -Electron Valence State Perturbation Theory: A Spinless Formulation and an Efficient Implementation of the Strongly Contracted and of the Partially Contracted Variants. *J. Chem. Phys.* **2002**, *117*, 9138.
38. *Molekel*, Advanced Interactive 3D-Graphics for Molecular Sciences, Swiss National Supercomputing Center. <https://ugovaretto.github.io/molekel/>
39. Stobie, K. M.; Bell, Z. R.; Munhoven, T. W.; Maher, J. P.; McCleverty, J. A.; Ward, M. D.; McInnes, E. J. L.; Totti, F.; Gatteschi, D. Mono- and Di-nuclear Tris(pyrazolyl)borato-oxo-Tungsten(V) Complexes with Phenolate Ligands: Syntheses and Structures, and Magnetic, Electrochemical and UV/Vis/NIR Spectroscopic Properties. *Dalton Trans.* **2003**, 36.
40. Young, C. G.; Enemark, J. H.; Collison, D.; Mabbs, F. E. The First Mononuclear Molybdenum(V) Complex with a Terminal Sulfido Ligand: $[\text{HB}(\text{Me}_2\text{C}_3\text{N}_2\text{H})_3]\text{MoSCl}_2$. *Inorg. Chem.* **1987**, *26*, 2925.
41. (a) Levason, W.; McAuliffe, C. A.; McCullough, F. P. Chemistry of Molybdenum and Tungsten. 10. Oxotungsten(V) and Oxotungsten(IV) Complexes of Diphosphine and Diarsine Ligands. *Inorg. Chem.* **1977**, *16*, 2911. (b) Jayarathne, U.; Chandrasekaran, P.; Greene, A. F.; Mague, J. T.; DeBeer, S.; Lancaster, K. M.; Sproules, S.; Donahue, J. P. X-ray Absorption Spectroscopy Systematics at the Tungsten L-Edge. *Inorg. Chem.* **2014**, *53*, 8230.

42. Nipales, N. S.; Westmoreland, T. D. Correlation of EPR Parameters with Electronic Structure in the Homologous Series of Low-Symmetry Complexes Tp^*MoOX_2 ($\text{Tp}^* = \text{Hydrotris}(3,5\text{-dimethylpyrazol-1-yl})\text{borate}$; $\text{X} = \text{F, Cl, Br}$). *Inorg. Chem.* **1997**, *36*, 756.
43. Mabbs, F. E.; Collison, D. *Electron Paramagnetic Resonance of d Transition Metal Compounds*; Elsevier: Amsterdam, 1992.
44. (a) Balagopalakrishna, C.; Kimbrough, J. T.; Westmoreland, T. D. Electronic Structural Contributions to g Values and Molybdenum Hyperfine Coupling Constants in Oxyhalide Anions of Molybdenum(V). *Inorg. Chem.* **1996**, *35*, 7758. (b) Swann, J.; Westmoreland, T. D. Density Functional Calculations of g Values and Molybdenum Hyperfine Coupling Constants for a Series of Molybdenum(V) Oxyhalide Anions. *Inorg. Chem.* **1997**, *36*, 5348.
45. (a) Gohr, S.; Hrobárik, P.; Kaupp, M. Four-Component Relativistic Density Functional Calculations of EPR Parameters for Model Complexes of Tungstoenzymes. *J. Phys. Chem. A* **2017**, *121*, 9106. (b) Wodyński, A.; Kaupp, M. Density Functional Calculations of Electron Paramagnetic Resonance g- and Hyperfine-Coupling Tensors Using the Exact Two-Component (X2C) Transformation and Efficient Approximations to the Two-Electron Spin–Orbit Terms. *J. Phys. Chem. A* **2019**, *123*, 5660.